Article:
Song, S, Yang, J, Ai, D et al. (7 more authors) (2019) Patch-Based Adaptive Background Subtraction for Vascular Enhancement in X-Ray Cineangiograms. IEEE Journal of Biomedical and Health Informatics, 23 (6). pp. 2563-2575. ISSN 2168-2194

https://doi.org/10.1109/jbhi.2019.2892072

Patch-based Adaptive Background Subtraction for Vascular Enhancement in X-ray Cineangiograms

Shuang Song, JianYang*, Danni Ai*, Chenbing Du, Yong Huang, Hong Song, Luosha Zhang, Yechen Han, Yongtian Wang, Alejandro F. Frangi, *IEEE Fellow*

***Abstract*— *Objective:* Automatic vascular enhancement in X-ray cineangiography is of crucial interest, for instance, for better visualizing and quantifying coronary arteries in diagnostic and interventional procedures. *Methods:* a novel patch-based adaptive background subtraction method (PABSM) is proposed automatically enhancing vessels in coronary X-ray cineangiography. First, pixels in the cineangiogram is described by the vesselness and Gabor features. Second, a classifier is utilized to separate the cineangiogram into the rough vascular and non-vascular region. Dilation is applied to the classified binary image to include more vascular region. Third, a patch-based background synthesis is utilized to fill the removed vascular region. *Results:* a database containing 320 cineangiograms of 175 patients was collected, and then an interventional cardiologist annotated all vascular structures. The performance of PABSM is compared with six state-of-the-art vascular enhancement methods regarding the precision-recall curve and C-value. The area under the precision-recall curve is 0.7133, and the C-value is 0.9659. *Conclusion:* PABSM can automatically enhance the coronary artery in the cineangiograms. It preserves the integrity of vascular topological structures, particularly in complex vascular regions and removes noise caused by the non-uniform gray level distribution in the cineangiogram. *Significance:* PABSM can avoid the motion artifacts and eases the subsequent vascular segmentation, which is crucial for the diagnosis and interventional procedures of coronary artery diseases.**

***Index Terms*—Learning, Adaptive Background, Enhancement, Coronary Cineangiography**

I. Introduction

Coronary artery disease (CAD) is a major threat to human health and is also one of the leading causes of death worldwide [1]. Due to the high spatial and temporal resolution, X-ray cineangiography remains the gold standard for diagnostic and interventional procedures of CAD [2]. However, owing to the projective nature of X-ray cineangiography [3], overlapping anatomical structures and intersecting vascular segments hamper precise measurement of vascular parameters. To date, numerous methods have been proposed to improve the accuracy of vascular segmentation [4], which are critical for quantifying vascular abnormality or choosing optimal treatment. Nevertheless, these techniques still lack robustness and accuracy to deal with image artifacts, complex vascular anatomy, non-uniform contrast filling, and confounding neighboring anatomy. In addition, the rapid wash out of contrast agent, heart motion, respiratory movement, and camera motion all may also considerably decrease the quality of cineangiograms and make vascular segmentation challenging. By removing undesired intensity variation and suppressing non-vascular structures and noise, vascular enhancement of cineangiograms can significantly ease subsequent vascular segmentation [5, 6]. This is the main goal of this work.

Hence, this paper proposes a novel patch-based adaptive background subtraction method (PABSM) to enhance the coronary artery from single live cineangiograms. Our approach addresses problems of previous approaches that process live cineangiograms (i.e. do not enhance background noise) yet also overcome limitations subtraction-based techniques (i.e. motion correction and mask frame selection). Vesselness and Gabor features are firstly calculated to describe center pixels at image patches. Probabilistic boosting tree is introduced to recognize vascular structures in the cineangiogram. After dilating the recognized vascular region and removing it from the cineangiograms, a virtual background is adaptively synthesized based on the intensity and edge information of the pixels in the remaining regions. We subtract the background from the coronary cineangiograms, and then enhance vascular structures by linear mapping of the gray values in the subtracted images.

The contributions of this paper are twofold:

1) We propose a new background synthesis method by combining the intensity and edge information. It is optimized within a neighbor region, which can ensure the continuity of gray values in the weak texture region, improve the continuity of edges in the ribs and diaphragm and the time efficiency.
2) We rigorously validate the proposed method quantitatively using phantom data from XCAT and 30 clinical cineangio-

This work was supported by The National Key Research and Development Program of China (2017YFC0107900), and the National Science Foundation Program of China (61672099, 81627803, 61501030, 61527827). AFF was partially funded by the Engineering and Physical Sciences Research Council (EP/N026993/1), the Royal Society International Exchanges Program (IE141258), and the European Commission (H2020-SC1-PM-16-2017-777119). (Corresponding author: Jian Yang, Danni Ai.)

Shuang Song, Jian Yang*, Danni Ai*, Chenbing Du, Yong Huang, Yongtian Wang are with the Beijing Engineering Research Center of Mixed Reality and Advanced Display, School of Optics and Photonics, Beijing Institute of Technology, Beijing 100081, China (e-mail: jyang@bit.edu.cn, Danni@bit.edu.cn).

Hong Song is with the School of Computer Science & Technology, Beijing Institute of Technology, Beijing 100081, China.

Luosha Zhang is with the Academy of Opto-Electronics, Chinese Academy of Sciences, Beijing 100081, China.

Yechen Han is with Department of Cardiology, Peking Union Medical College Hospital, Beijing 100730, China.

Alejandro F Frangi is with the Center for Computational Imaging and Simulation Technologies in Biomedicine (CISTIB), School of Computing and School of Medicine, University of Leeds, Leeds LS2 9JT, UK.

grams from 30 different patients. The results show that our proposed method can effectively avoid the motion artifacts, ribs, diaphragm and other non-vascular structures and also preserve the integrity of vascular topological structures.

II. Related Work

For angiographic imaging technology, images obtained during and prior to passage of contrast agent are referred to as live and mask cineangiograms, respectively. Differential operators directly applied to live cineangiograms are most extensively used in vascular enhancement: first derivatives are utilized to extract vascular edges, whereas second derivatives are utilized to describe their local curvature or shape. The structure tensor [7-9], Weingarten matrix [10], and Hessian matrix [11-13] are all widely applied to enhance blob, tubular, and plane-line structures. In the most famous vesselness based method [11], the authors convolved the input image with the derivatives of a Gaussian kernel at multiple spatial scales, and then compute and analyze the Hessian matrix response at each pixel to distinguish tubular structures from blob-like structures. However, due to the suppression of junctions, the vessel network usually shows undesirable discontinuities. Subsequently, Jerman et al. [14] proposed the enhancement of vessels using the multi-scale ratio of the Hessian eigenvalues. In this method, the multi-scale response of the filter can yield a close-to-uniform response in all scales of vascular structures.

However, as contrast agent induces non-uniform intensity in the cineangiograms, the method should also be adaptive to different blurring effects of the boundary and different levels of the image noise. Qian et al. [15] directly enhanced the vasculature by extracting all pixels that satisfy the statistical characteristics of local intensity profile. Though the method enables the detection of vessels near the complex extreme structures, the enhanced result still considerably depends on the image intensity. Lathen et al. [16] proposed the local phase-based filter, where the local phase information is extracted using the quadrature filters. This method can effectively enhance vessels with different widths and preserve the sharpness of the vessel boundaries.

The previous methods process individual live cineangiograms and, consequently, will inevitably enhance both vascular contrast and background noise. Subtraction based background removal methods [17-19] are more attractive as they combine information from both live and mask cineangiograms to achieve selective vessel enhancement. Feature-based methods have been extensively studied for background subtraction, where the matched patches between the live and mask cineangiograms can be computed by a similarity metric-based template matching [20]. Vascular enhancement is achieved by subtracting the deformed mask image from the live image. The methods usually cannot remove the skeleton structures and the diaphragm. To further reduce the false matched points, Zhu et al. [21, 22] built a classifier using Haar features to coarsely separate the live cineangiogram into vessel and non-vessel regions. They obtain the matched points in the mask over the live cineangiograms using the local optical flow method. Since the local optical flow cannot accurately estimate the matched points in weak texture regions, most non-uniform illumination cannot be removed.

Another kind of subtraction-based methods refers to the layer separation. Robust principal component analysis, and related variants, are also utilized to realize the background separation in the cineangiograms [5, 23]. By assuming the cineangiogram is comprised of low rank and sparse layers, a target function is gradually optimized across a cineangiograms sequence to obtain optimal sparse layers. The sparse layer of each cineangiogram in the sequences represents a subtraction image. Comparing with the methods directly processing the live cineangiogram, subtraction-based methods can remove substantial background noise while maintaining accurate vascular information. However, the deformed mask cineangiogram cannot reflect the exact background of the live cineangiogram, which limits the ability of denoising. On the other hand, subtraction based methods also suffer from the limitation of adequately selecting the mask frame and updating it as it becomes obsolete (e.g. due to patient or table motion). Motion artifacts [24] can lead to spurious features being created in the subtraction image that can lead to misdiagnosis or clutter the vasculature of interest with unwanted features.

For the single-frame based background removal methods, morphological closure [25] or top-hat filtering [26] has been utilized. However, considering the multi-structures co-exist in the angiogram, the non-vascular structures cannot be removed completely. Unberath et al.[27-29] generated binary segmentation masks by merging the responses of the vesselness- and Koller-filtering, and utilized patch-wised spectral inpainting to fill the segmented pixels to compute the virtual mask cineangiograms. The final enhanced vascular image was obtained by subtracting the virtual mask from the original live cineangiograms. To accurately compute the virtual mask when large areas need to be inpainted, Unberath et al. [30] again trained a U-net to estimate the virtual mask. When the vessels are overlapped with the diaphragm, lung tissues or vertebral bodies, the inpainted vascular region can be cluttered by the structures.

III. Methodology

The flowchart of the proposed PABSM is illustrated in Fig. 1. In this method, vascular detection is utilized to detect the pixels that belong to the vascular structures and generate a defect image that can reveal the unknown region. Background synthesis is exploited to obtain a virtual background which is very similar to the real mask cineangiogram. The final subtraction cineangiogram, that contains the vascular structures with high contrast, is computed by subtracting the virtual background from the original cineangiogram.

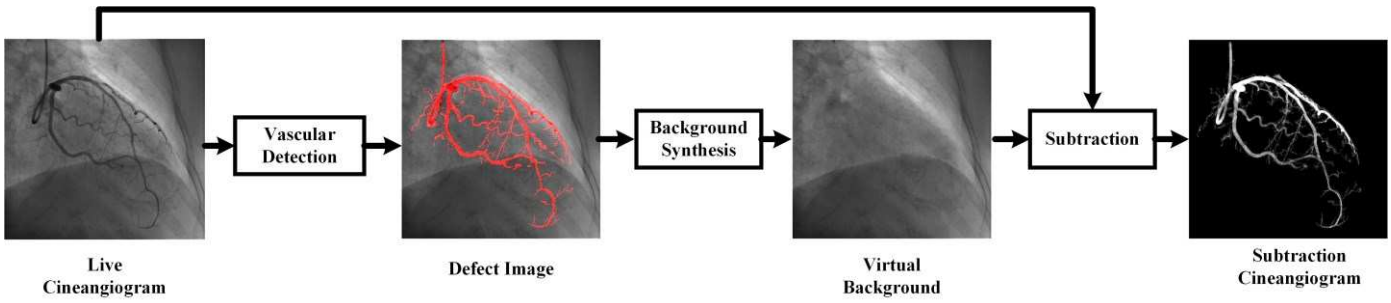

Fig. 1. Flowchart of the proposed method.

A. Pixel Description

To improve the accuracy of vascular detection, the pixels in the cineangiogram should be described by feature vectors. Before the feature extraction, based on the sparseness property of gradient probability distributions [31], the non-uniform intensity distribution in the cineangiograms is firstly corrected and the vascular information can also be preserved. In the corrected image $\mathbf{I}$, we denote the k^{th} pixel centered image patch as $\mathbf{P}_k$. Two kinds of features are extracted for describing the center pixel in the image patch based on the vesselness and Gabor features.

The vesselness map $\mathbf{V}(\mathbf{P}_k)$ of an image patch [11] is computed to distinguish blob-like structures and suppress background noise:

$$\mathbf{V}(\mathbf{P}_k) = \max(\{\mathbf{V}_k(e_1)|e_1 = 1, \cdots, E_1\}), \quad (1)$$

where $\mathbf{V}_k(e_1)$ is the vesselness map of k^{th} image patch at scale e_1. Then, the center pixel of the k^{th} image patch can be described by the mean and standard deviation values of the vesselness map:

$$(f_{k,1},\ f_{k,2}) = \left(\text{mean}(\mathbf{V}(\mathbf{P}_k)), \text{std}(\mathbf{V}(\mathbf{P}_k))\right), \quad (2)$$

where $\text{mean}(\cdot)$ is the mean of $\mathbf{V}(\mathbf{P}_k)$; $\text{std}(\cdot)$ is the standard deviation of $\mathbf{V}(\mathbf{P}_k)$.

To make the vascular detection invariant to rotation, scaling and translation transformations, and to improve the robustness against photometric variations, Gabor filters [32] are also applied to image patches as:

$$\mathbf{G}_{e_2,m}(\mathbf{P}_k) = \mathbf{P}_k * \mathbf{G}_{e_2,m},\ e_2 = 1, \cdots, E_2; m = 1, \cdots, M, \quad (3)$$

where $\mathbf{G}_{e_2,m}(\mathbf{P}_k)$ is the filtered patch by the Gabor filter $\mathbf{G}_{e_2,m}$; m represents the orientation of the normal to the parallel stripes of a Gabor function; $*$ refers to the convolution. The center pixel of the k^{th} patch can be described the mean and standard deviation values of $\mathbf{G}_{e_2,m}(\mathbf{P}_k)$:

$$\begin{aligned} f_{k,2\times e_2\times m-1} &= \text{mean}\left(\mathbf{G}_{e_2,m}(\mathbf{P}_k)\right) \\ f_{k,2\times e_2\times m} &= \text{std}\left(\mathbf{G}_{e_2,m}(\mathbf{P}_k)\right) \end{aligned}. \quad (4)$$

Till now, the center pixel of each image patch is described by a feature vector with $2 \times (e_2 \times m + 1)$ dimension, which is denoted as $\mathbf{f}_k$.

To reduce the computation load of subsequent classification on a live cineangiogram, the key points (KPS) are extracted. In extracting KPS, the cineangiogram is initially enhanced by a vesselness filter[11]. Then, for each pixel in the enhanced cineangiogram, the eigenvalue λ_1 of the Hessian matrix is computed and the corresponding eigenvector v_1 is along the tangential direction of the vascular centerline. Considering Xiao et al.[33] has demonstrated that the pixels belong to a tubular structure when eigenvalue $\lambda_1 < 0$, we compute the largest connected region of pixels whose eigenvalue $\lambda_1 < 0$. In addition, the pixels in the obtained region comprise the KPS. Fig. 2. shows the example of the extracted KPS in the cineangiograms.

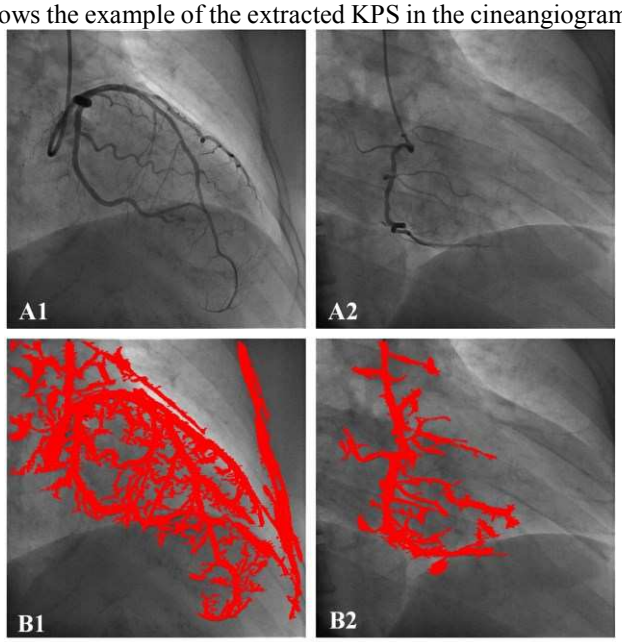

Fig. 2. Example of the extracted KPS in the cineangiograms. (A1 and A2) live cineangiogram; (B1 and B2) extracted KPS of left and right coronary artery, respectively (pixels in red).

B. Vascular Region Detection

Since the KPS contains large amounts of non-vascular pixels, probabilistic boosting tree (PBT) [34] is utilized to distinguish the non-vascular pixels. PBT is a tree-like classifier with Adaboost [35] as node classifier. In training PBT, We describe the training set as $\{(\mathbf{f}_k, l_k, w_k)|l_k \in \{-1,1\}\}, k = 1, \cdots, K$, where w_k is the weight of $\mathbf{f}_k$, and $\sum_k w_k = 1$, K is the number of $\mathbf{f}_k$ in the training set. The training set is divided into two child nodes from the current node according to the following principle:

$$\begin{cases} (\mathbf{f}_k, l_k, 1) \to n_{right} & q(+1|\mathbf{f}_k) - \frac{1}{2} > \varepsilon \\ (\mathbf{f}_k, l_k, 1) \to n_{left} & q(-1|\mathbf{f}_k) - \frac{1}{2} > \varepsilon \\ \begin{cases} (\mathbf{f}_k, l_k, q(+1|\mathbf{f}_k)) \to n_{right} \\ (\mathbf{f}_k, l_k, q(-1|\mathbf{f}_k)) \to n_{left} \end{cases} & otherwise \end{cases}, \quad (5)$$

where n_{left} and n_{right} represent the left and right child nodes of the current node; $q(+1|\mathbf{f}_k)$ and $q(-1|\mathbf{f}_k)$ are the probabilities of the feature vector $\mathbf{f}_k$ after the Adaboost classification in node; l_k is the label of training pixels; $l_k = 1$ corresponds to the pixels of vessels while $l_k = -1$ to the pixels of background; ε is utilized to control the over-fitting of the classification. In each level, $\{w_k\}$ are normalized. Eq.5 is repeated if the depth of the tree is un-reached or the errors of the classifier in the nodes are within a threshold value.

For a test feature, the posterior probability $\tilde{q}(l_k|\mathbf{f}_k)$ of $\mathbf{f}_k$ can be computed as [34]:

$$\tilde{q}(l_k|\mathbf{f}_k) = \sum_h \big(\tilde{q}\big(l_k|l_{H,k}, \cdots, l_{1,k}, \mathbf{f}_k\big), \cdots, q\big(l_{h,k}|l_{h-1,k}, \cdots, l_{1,k}, \mathbf{f}_k\big), \cdots, q\big(l_{1,k}|\mathbf{f}_k\big)\big), \quad (6)$$

where $q\big(l_{1,k}|\mathbf{f}_k\big)$ and $q\big(l_{h,k}|l_{h-1,k}, \cdots, l_{1,k}, \mathbf{f}_k\big)$ are the computed probability by the classifier of the nodes in the first and next h^{th} level.

Thereafter the label l_k of $\mathbf{f}_k$ are decided by the threshold value ζ, as follows:

$$l_k = \begin{cases} 1 & \tilde{q}(l_k|\mathbf{f}_k) \geq \zeta \\ -1 & \tilde{q}(l_k|\mathbf{f}_k) < \zeta \end{cases}. \quad (7)$$

For a live cineangiogram, after finishing the classification of the pixels, we obtained a vascular binary image. However, some pixels distributed near the vascular boundary or with small diameters may also be misclassified as background noise. Hence, after finding the largest connection region in the binary image, the binary image is dilated to include the vascular boundary and missed region in the vessels. The final defect image $\mathbf{I}_1$ is obtained by removing the dilated vascular regions from $\mathbf{I}$.

C. Patch-based Background Synthesis and Subtraction

We regarded the non-vascular region in $\mathbf{I}_1$ as the known region while the removed vascular region as unknown regions. Background synthesis is to compute a virtual mask cineangiogram by filling the unknown region by the patches in the known region. By subtracting the virtual mask cineangiogram from the original live cineangiogram, the vascular structures can be enhanced. Since much weak texture region, ribs and diaphragm exist in the cineangiogram, the background synthesis should ensure the continuity of gray values within these structures. To ensure the continuity of gray values in the weak texture regions, the energy of the histogram differences (EHD) is utilized to compute the difference of gray values of the patches in the known and unknown regions. To improve the continuity of edges, the edge difference between the patches in the known and unknown regions is regarded as the second constraint. In the optimization of the background synthesis, the optimal matching patches in the unknown region may occur in different region of cineangiogram. To avoid searching for the patches which have large difference with the patches in the unknown regions, the neighbor-region-searching is the third constraint. It can also improve the time efficiency. Hence, the background synthesis of computing $\mathbf{I}_2$ takes the form:

$$\operatorname{argmin}_{\{\mathbf{H}_u\}} \sum_{u \in \widehat{\Omega}} \big(\omega_1 * E_1(\mathbf{H}_u(\mathbf{s}_u), \mathbf{t}_u) + \omega_2 * E_2(\mathbf{H}_u(\mathbf{s}_u), \mathbf{t}_u) + \omega_3 * E_3(\mathbf{s}_u, \mathbf{t}_u)\big), \quad (8)$$

where $\widehat{\Omega}$ is the pixel indices of the unknown region in $\mathbf{I}_1$. Here, $\mathbf{t}_u = \big(t_u^x, t_u^y, 1\big)$ is the homogeneous center coordinates of the target in the unknown region, and $\mathbf{s}_u = \big(s_u^x, s_u^y, 1\big)$ is the homogeneous center coordinates of a source patch in the known region. $\mathbf{H}_u(\cdot)$ represents the transformation for the matched source patch to smooth the filled unknown region. We assume this transformation is affine in this paper. The weight values ω_1, ω_2 and ω_3 are utilized to balance each function $E_1(\cdot)$, $E_2(\cdot)$ and $E_3(\cdot)$, and $\omega_1 + \omega_2 + \omega_3 = 1$.

$E_1(\cdot)$ represents the intensity difference between the transformed source patch and the target patch to measure their similarities:

$$E_1(\mathbf{H}_u(\mathbf{s}_u), \mathbf{t}_u) = \sum_{z=-Z}^{Z} \Big(\frac{1}{N^2} \sum_{dx,dy} \delta\Big(\mathbf{I}_1\big(\mathbf{H}_u(s_u^x + dx, s_u^y + dy)\big) - \mathbf{I}_1\big(t_u^x + dx, t_u^y + dy\big)\Big), z\Big)^2, \quad (9)$$

where dx and dy are the offsets of pixels in the $\big(s_u^x, s_u^y\big)$ centered patch; $z \in [-Z, Z]$ is the intensity distribution of the difference of the transformed patch and the target patch; N is the number of pixels in the patches; $\delta(\cdot)$ is a sign function.

E_2 describes the difference of the edge map between the transformed source patch and the target patch, which is:

$$E_2(\mathbf{H}_u(\mathbf{s}_u), \mathbf{t}_u) = \frac{1}{N^2} \Big(\sum_{dx,dy} d\Big(\mathbf{H}_u\big(s_u^x + dx, s_u^y + dy\big)\Big) - d\big(t_u^x + dx, t_u^y + dy\big)\Big), \quad (10)$$

where $d(\cdot)$ refers to the edge value. In the estimation of the edge map of $\mathbf{I}_1$, a four-order Sobel operator is applied to $\mathbf{I}_1$. By setting the edge of the pixels belong to the unknown region in $\mathbf{I}_1$ as 0, the edge map is computed. Fig. 3 shows the extracted edge of Fig. 2(B1) and (B2).

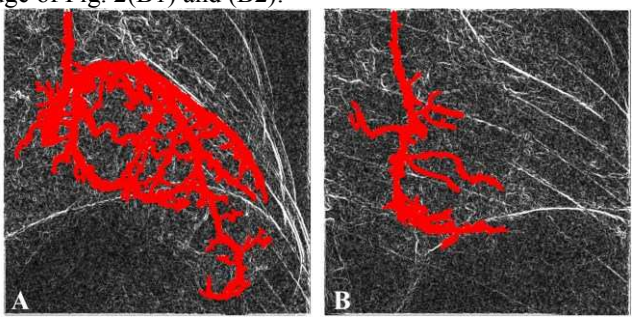

Fig. 3. Extracted edge of Fig. 2(B1) and (B2), respectively.

$E_3(\cdot)$ is utilized to constrain the search space to the neighbor regions of $\mathbf{t}_u$, and is expressed as follows [36]:

$$E_3(\mathbf{s}_u, \mathbf{t}_u) = \frac{\|\mathbf{t}_u - \mathbf{s}_u\|_2^2}{\gamma(\mathbf{t}_u) + \tau^2}, \quad (11)$$

where $\gamma(\mathbf{t}_u)$ is the squared distance between $\mathbf{t}_u$ and the border of the known region. τ is a constant to adjust the strength of the proximity constraint. Eq. (8) is optimized by the random location sampling in the PatchMatch algorithm [37]. And the sampling range is restricted in the neighbor region of the unknown regions. The adaptive background $\mathbf{I}_2$ is finally synthesized by filling the target patch in the unknown region of $\mathbf{I}_1$. Fig. 4 shows the example including the original cineangiogram $\mathbf{I}$, defect image $\mathbf{I}_1$ and the synthesized background $\mathbf{I}_2$.

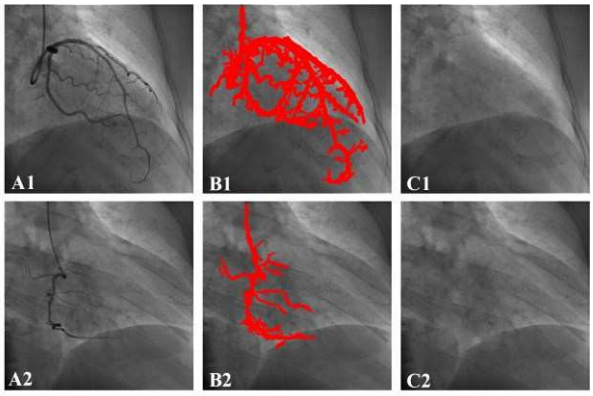

Fig. 4. Examples of the original cineangiogram **I**, defect image $\mathbf{I}_1$, and the synthesized background $\mathbf{I}_2$.

The difference between the original cineangiogram **I**, and the adaptive background image $\mathbf{I}_2$ could effectively remove the background structures and extract vascular structures.

Hence, according to the X-ray imaging principle [38], the subtraction image can be computed as follows:

$$\mathbf{I_3} = exp\big(ln(\mathbf{I}) - ln(\mathbf{I_2})\big). \quad (12)$$

Since the difference of vascular structures in $\mathbf{I}_3$ between the vessels and background is greatly reduced after the subtraction, linear mapping is then utilized to improve the visualization of vessels by computing a linear transformation matrix. The matrix is calculated by transforming the minimum and maximum range to a specific output range.

D. Implementation Details

The algorithm for PABSM can be summarized as the following pseudocode (TABLE I).

TABLE I
Pseudocode of PABSM.

Input: labeled patches from C-AED, live cineangiograms from PABSM-AED
Output: subtraction cineangiograms

Classifier training:
1: calculate the feature vector $\mathbf{f}_k$ of each patch;
2: train the PBT classifier;
PABSM:
1: calculate the KPS of cineangiogram **I**;
2: calculate the feature vector $\mathbf{f}_k$ of each key-point-centered patch;
3: classify the patches by the trained classifier;
4: dilate the obtained binary classification image;
5: calculate $\mathbf{I}_1$ by removing the pixels in the dilated region from **I**;
6: calculate the edge map of $\mathbf{I}_1$;
7: calculate $\mathbf{I}_2$ by performing the background synthesis by (8) on $\mathbf{I}_1$;
8: calculate $\mathbf{I}_3$ by subtracting $\mathbf{I}_2$ from **I**.
return $\mathbf{I}_3$.

IV. Experiment

A. Datasets

1) Phantom Data

To evaluate the proposed PABSM quantitatively, we perform the simulation of live cineangiogram based on the XCAT [39]. We simulate the 3D volume data with and without the non-vascular structures. The cineangiograms are computed by a perspective projection model [40]. The cineangiograms only with vascular structures can be regarded as the ground truth of vessels in the cineangiograms that contain non-vascular structures to enable the evaluation of vascular enhancement. The source-to-detector and source-to-isocenter distances are set to 1100mm and 780mm, respectively. Each cineangiograms has 450×450 pixels with a resolution of 0.3×0.3 mm.

2) Clinical Data

The proposed method was evaluated on a database of cineangiograms collected from an on-going coronary artery study in collaboration with the Peking Union Medical College Hospital. The database is divided into two data sets: (1) classifier accuracy evaluation dataset (C-AED) and (2) PABSM accuracy evaluation dataset (PABSM-AED). Each cineangiogram has a size of 512×512 pixels and the resolution is 0.3×0.3 mm.

C-AED contains 290 images with 145 left and 145 right coronary cineangiograms, and is utilized for the accuracy evaluation of the classifier PBT. The data set is from 145 patients; for each patient, two cineangiograms at different cardiac phases are selected. For each cineangiogram, an interventional cardiologist with 15 years of experience in interventional radiology roughly annotated vascular boundaries. The interior of the annotated area is the vascular region, whereas the exterior area is the non-vascular region. We use a skeleton thinning method to acquire the centerline in the vascular region. The points belong to the centerline are the center of the extracted vascular patches from the cineangiograms. To extract the image patches of non-vascular regions, the vascular region is dilated by an element size of 7×7 pixels. Points between the image border and the boundary 7 pixels away from the edge of the dilated regions are sampled as the center of the extracted non-vascular patches. A total of 517,490 patches are extracted consisting of 199,800 vascular patches, and 317,690 non-vascular patches.

PABSM-AED includes 30 live and 30 mask cineangiograms from different patients, with 19 left and 11 right coronary arteries. For each patient, a mask and a live cineangiogram are selected. For each live cineangiogram, the ground truth was detailed annotated by an interventional cardiologist with 15 years of experience in coronary artery disease. For each mask cineangiogram, the labeled regions in the live cineangiograms are removed from the corresponding mask cineangiograms. Labeled mask cineangiograms in PABSM-AED is utilized to evaluate the proposed background synthesis. While the live cineangiograms in PABSM-AED is utilized to evaluate the performance of the proposed PABSM. For each live cineangiogram in the dataset, to improve the time efficiency and accuracy of the classification, KPS are initially extracted before the classification. The corresponding patches of the KPS are generated by regarding the KPS as the center pixel. Fig. 5 shows several ground

truth in PABSM-AED.

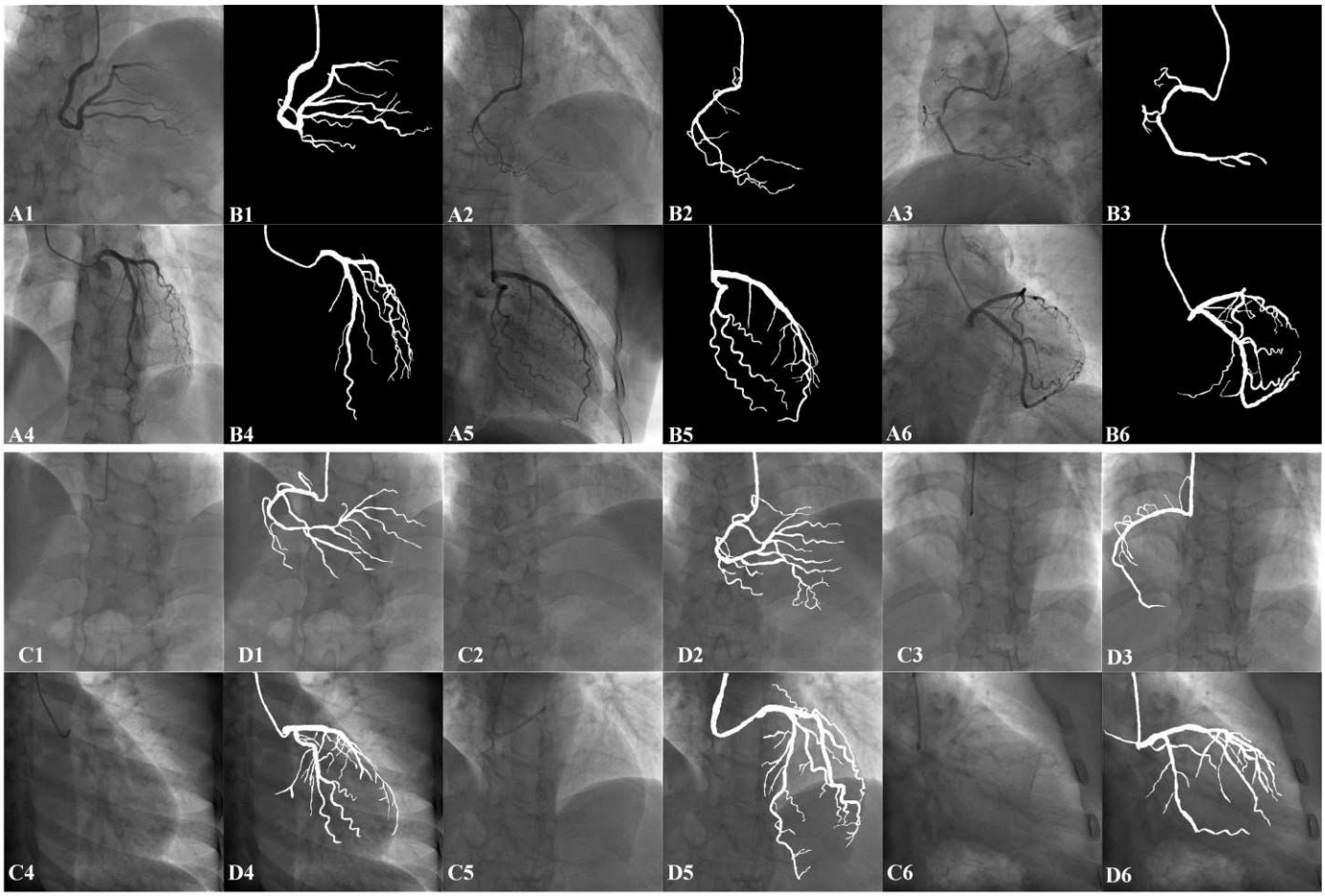

Fig. 5. The ground truth in PABSM-AED. (A1-A6) Original live cineangiograms; (B1-B6) labeled live cineangiograms; (C1-C6) original mask cineangiograms; (D1-D6) labeled mask cineangiograms.

B. Experiment Design

10-fold cross validation is performed to evaluate the classifier: the training and test cycles are repeated 10 times, and in each iteration, 465,741 and 51,749 patches comprise the training and test sets, respectively. Next, the obtained classifier is applied to the live cineangiograms in PABSM-AED to detect the vascular region. To evaluate the effectiveness of KPS extraction, we will qualitatively compare the subtraction results with and without KPS.

The proposed patch-based background synthesis method will be compared with the spectral based method (SBM) [28] using the mask cineangiograms in PABSM-AED. We also conduct a series of experiments to evaluate the influence of parameters ω_1, ω_2 and ω_3 to the accuracy of background synthesis. The Structural Similarity (SSIM) and Root-Mean-Square Error (RMSE) are utilized to compare the synthesized backgrounds with the original mask cineangiograms.

The proposed PABSM will be compared with method, namely, line-based [41], local phase-based [16] and BCOSFIRE-based methods [13] (LBM, LPBM, and BBM) on both of the phantom data and clinical data. The aim is to evaluate the preservation of local structures. Since PABSM is inspired from the subtraction-based methods, PABSM will also be compared with methods, namely, multi-resolution registration-based method (MRRBM) [42], motion coherency constraint-based method (MCCBM) [23] and stochastic optimization-based method (SOBM) [5]. The precision-recall curve is utilized to quantitatively evaluate the preservation of vascular structures in the images obtained by the methods, namely, LBM, LPBM, BBM, MRRBM, MCCBM, SOBM and the proposed PABSM, on clinical data. The precision and recall ratios are computed using the following equations, respectively:

$$\text{Precision} = \frac{tp}{tp+fp}, \tag{13}$$

$$\text{Recall} = \frac{tp}{tp+fn}, \tag{14}$$

where tp, fp, fn indicate true positive (correctly identified vessel pixels), false positive (incorrectly identified vessel pixels), and false negative (incorrectly identified background pixels), respectively. In addition, we also compute C-value to denote the contrast between the target structure and background noise. C-value is computed using the following equation:

$$\text{C} = \left|\frac{F-B}{F+B}\right|, \tag{15}$$

where F and B represent the average gray value of the target structure and background region, respectively.

MRRBM requires a mask and a live cineangiograms which have the most similar cardio-respiratory motion. MRRBM is re-implemented in strict accordance with the original paper.

MCCBM utilizes structural connectivity and robust principal component analysis (RPCA) to extract a rough vascular layer. Then trajectory decomposition is employed to obtain an accurate vascular layer. SOBM utilizes a morphological operator to obtain a rough vascular layer. Then online RPCA is utilized to separate the rough vascular layer into a static layer and an accurate vascular layer. We achieve MCCBM[1] and SOBM[2] using available public implementations. MCCBM and SOBM are both applied in a cineangiographic sequence. SOBM is online while MCCBM is not.

C. Results

All the algorithms were implemented in C++ under the Ubuntu environment, and all the experiments were conducted on a relatively low-cost PC with 16 GB RAM and 3.2 GHz Intel CPU.

An overview of the parameters in the proposed PABSM is given in Table II. The scales of the pixel description are set according to the vascular diameters. The directions of Gabor filter in pixel description ensure the possible vascular directions. Parameter ε in the classification is decided by the overlapping range of the computed probability of vascular and non-vascular patches in the first node of the classifier. The weight values in the background synthesis are optimal on the mask cineangiograms from the same sequence in PABSM-AED.

TABLE II
Parameter setting used in the proposed PABSM.

Parameters		values
Pixel Description	E	5
	M	8
Vascular detection	ε	0.001
	ζ	0.5
Background Synthesis	ω_1	0.85
	ω_2	0.05
	ω_3	0.1
	Patch size	9×9

1) Evaluation of the Classifier

All experiments for the classifier evaluation are realized either over the full training or test sets. The average training accuracy of the 10-fold cross validation is $96.55\% \pm 0.06\%$, and the test accuracy is $92.52\% \pm 0.72\%$. The training accuracy of the 10-fold cross validation only on vesselness features is $76.38\% \pm 0.14\%$, and the test accuracy is $80.13\% \pm 2.13\%$. The training accuracy of the 10-fold cross validation only on Gabor features is $94.12\% \pm 0.08\%$, and the test accuracy is $85.23\% \pm 0.85\%$. The classifier based on both of vesselness and Gabor features has better ability to distinguish the vascular and non-vascular regions.

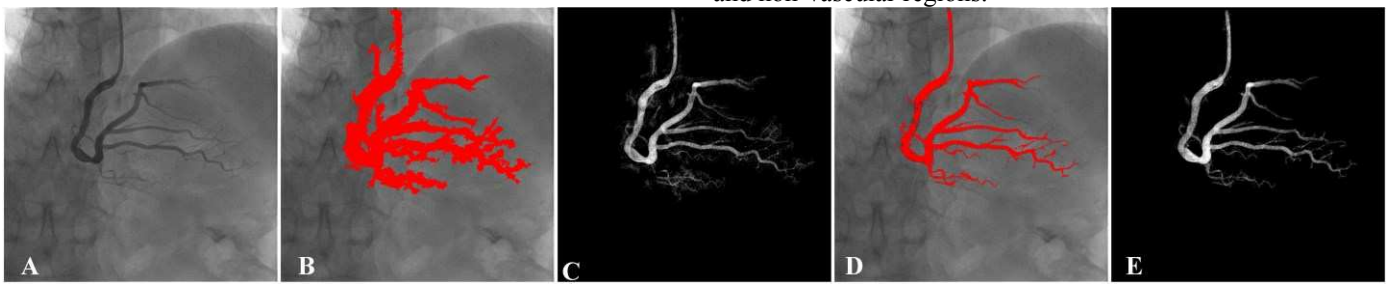

Fig. 6. Illustrative classification results using different point sampling methods and their later PABSM-based enhancement results. (A) Randomly selected image from PABSM-AED. (B and D) Classification results on (A) APS and KPS, respectively. (C and E) PABSM-based enhancement results on (B and D).

Fig. 6 shows an example of the enhancement results using the PABSM when a randomly selected image from PABSM-AED is classified using APS and KPS. Fig. 6(B) exhibits that APS tends to misclassify the pixels around the vascular boundary as vessels. For the KPS classification result (see Fig. 6(B)), the pixels around the vascular boundary are mostly removed and the vessels of the different scales are preserved, enabling the vessels to considerably stand out from the background. The enhancement results derived from the APS- and KPS-based classification are shown in Figs. 6(C), (E). As expected, numerous non-vascular structures are removed by the KPS-based classification. The PABSM ensures the accurate enhancement of the boundary.

2) Evaluation of the Background Synthesis

Considering that $E_3(\cdot)$ is utilized to constrain the search space to the neighbor regions of unknown patch, Table III shows the RMSE and SSIM of the synthesized background when ω_3 varies from 0 to 0.9. Meanwhile, the time of background synthesis are also shown in Table III to evaluate the influence of ω_3 to the time efficiency of background synthesis. As can be seen from Table III, the RMSE and SSIM are not influenced by ω_3. And when $\omega_3 = 0.1$, the time efficiency of background synthesis is the highest. By setting ω_3 as 0.1 , Figs 7 and 8 shows the RSME and SSIM when ω_1 and ω_2 varies. As can be seen from the figures, RMSE and SSIM are optimal when $\omega_1 = 0.85$, $\omega_2 = 0.05$, and both of RMSE and SSIM decrease when ω_2 increases. In addition, Table IV shows RMSE and SSIM when the patch size varies from 7×7 to 15×15 in the background synthesis. When the patch size is 9×9, both of RMSE and SSIM are optimal.

TABLE III
Changing of RMSE, SSIM and time with the increase of ω_3.
$\omega_1 = \omega_2 = (1 - \omega_3)/2$.

ω_3	RMSE	SSIM	Time(s)
0.0	2.03 ± 0.43	0.950 ± 0.032	14.15 ± 3.45
0.1	2.01 ± 0.41	0.951 ± 0.032	$\mathbf{12.23 \pm 3.00}$
0.2	2.00 ± 0.42	0.950 ± 0.032	12.89 ± 3.11
0.3	2.00 ± 0.41	0.950 ± 0.032	13.01 ± 3.42
0.4	2.00 ± 0.41	0.950 ± 0.032	13.12 ± 3.42
0.5	2.00 ± 0.41	0.950 ± 0.032	13.33 ± 3.51
0.6	2.00 ± 0.41	0.950 ± 0.032	13.62 ± 3.49
0.7	2.00 ± 0.41	0.950 ± 0.032	14.08 ± 3.99
0.8	2.00 ± 0.41	0.950 ± 0.032	14.54 ± 4.01
0.9	2.00 ± 0.41	0.950 ± 0.033	14.88 ± 5.34

[1] http://www.escience.cn/people/bjqin/research.html

[2] https://github.com/andrewssobral/lrslibrary

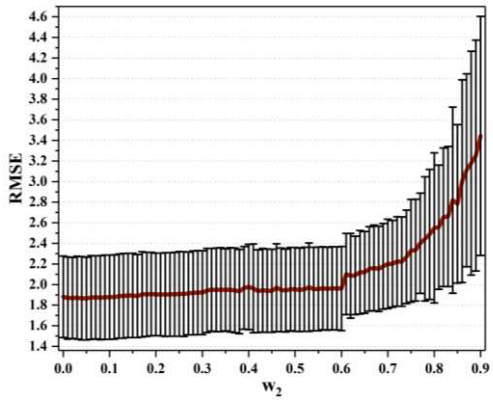

Fig. 7. Mean and standard deviation of RMSE along with the increase of ω_2, $\omega_1 + \omega_2 = 0.9$.

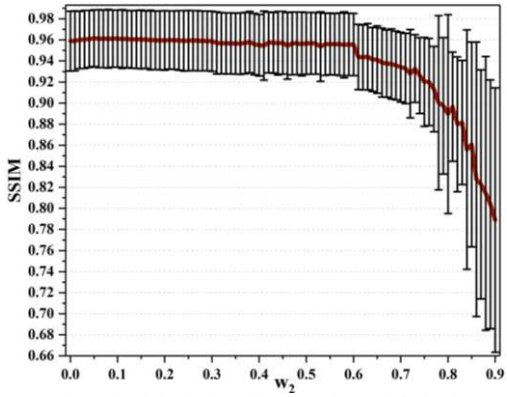

Fig. 8. Mean and standard deviation of SSIM along with the increase of ω_2, $\omega_1 + \omega_2 = 0.9$.

TABLE IV
Variation of RMSE and SSIM along with the increase of patch size in the background synthesis.

Patch Size	RMSE	SSIM
7×7	1.873 ± 0.40	0.960 ± 0.028
9×9	1.863 ± 0.40	0.962 ± 0.027
11×11	1.872 ± 0.40	0.960 ± 0.029
13×13	1.876 ± 0.40	0.955 ± 0.030
15×15	1.900 ± 0.41	0.948 ± 0.031

TABLE V
Background synthesis performance on the randomly mask cineangiograms from the sequences in PABMS-AED by SBM and the proposed methods, respectively.

Methods	SSIM	RMSE
SBM	0.934±0.031	2.696±0.44
Proposed	0.962±0.027	1.863±0.40

Fig. 9 shows the comparison results of the proposed method with SBM. SBM cannot ensure the intensity continuity. The proposed method can obtain the synthesized background with continuity intensity and edge. Table V shows the quantitative comparison results by the two background synthesis methods. The values of SSIM and RMSE of the proposed method are all better than SBM. It indicates that the proposed background synthesis method can effectively restore the background.

3) *Evaluation of the proposed PABSM*

Fig. 10 shows the enhancement results by the proposed PABSM on the phantom data. PABSM can effectively remove the non-vascular structures and preserve the vascular structures.

Fig. 11 shows the precision-recall curves by methods, namely, LBM, LPBM, BBM and PABSM. According to the order of LBM, LPBM, BBM and PABSM, the areas under the precision-recall curve are 0.0495, 0.5987, 0.0301 and 0.8806. As can be seen from Fig. 11, PABSM can obtain a high segmentation accuracy.

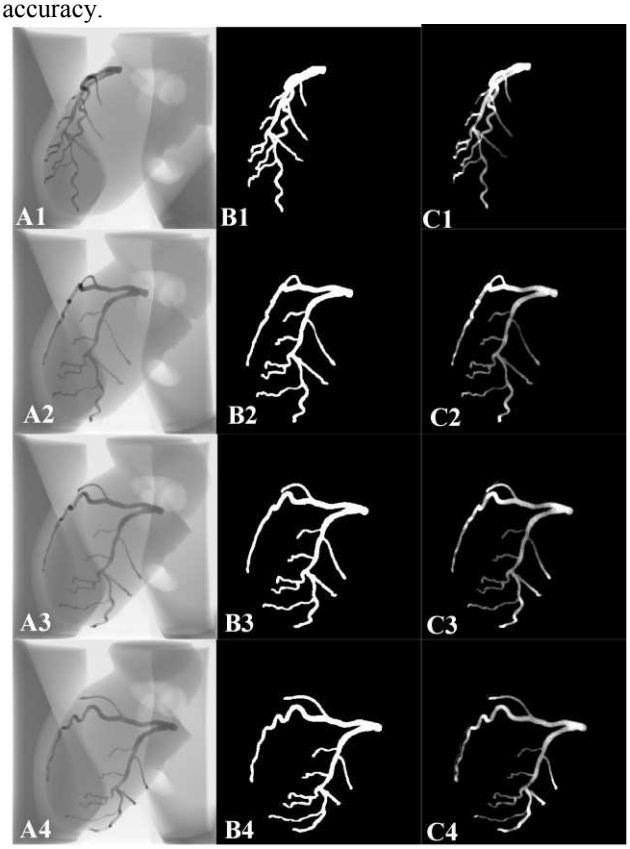

Fig. 10 Evaluation of proposed PABSM on the phantom data. (A1-A4) original live cineangiograms; (B1-B4) ground truth; (C1-C4) results by PABSM.

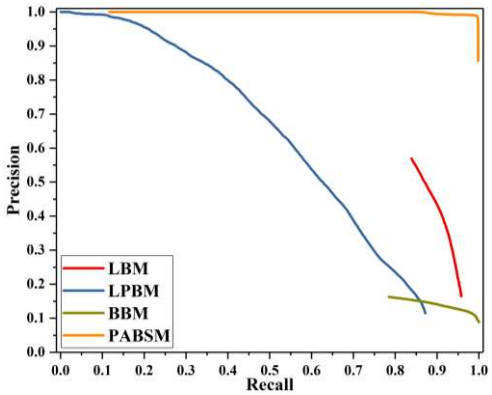

Fig. 11. Precision-recall curves of methods, namely, LBM, LPBM, BBM and the proposed PABSM.

Fig. 12 shows the enhancement results of three left coronary arteries and three right coronary arteries. The cineangiograms in Fig. 12 are collected from different cardiac phases of various patients. Figs. 12(B1-B6) shows that PBT can extract the vascular regions from different cineangiograms and suppress the background noise. The patch-based background subtraction results are unconstrained by the distribution and location of the vascular network (see Figs. 12(C1-C6)). In addition, the proposed method can effectively guarantee the continuity of the

vessels with their surrounding neighborhood regions. Figs. 12(D1-D6) show that the enhanced vessels preserve the information of the vascular bifurcations, branches, and vascular boundary. The region contains the overflow of contrast agent is substantially reduced or eliminated. Therefore, PABSM is robust for the enhancement of the cineangiograms with different vascular structures.

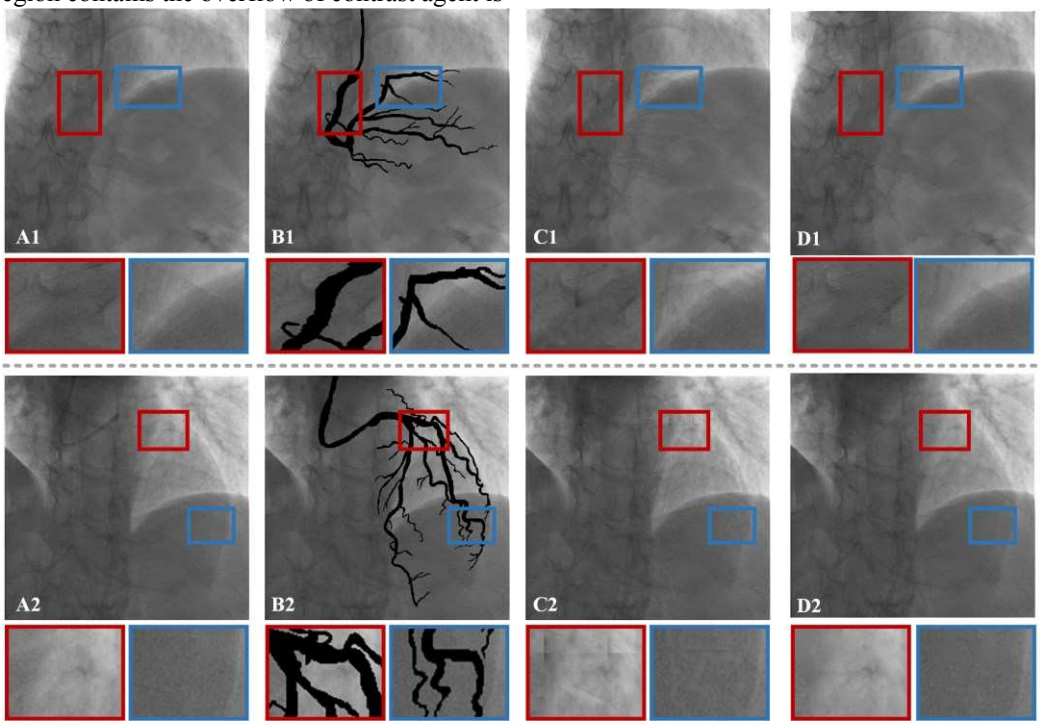

Fig. 9. Illustrative results of background synthesis by different methods. (A1 and A2) original mask cineangiograms; (B1 and B2) defect cineangiograms; (C1 and C2, D1 and D2) synthesized background by SBM and the proposed method, respectively. Second row: enlarged views of interest in first row; Fourth row: enlarged views of interest in third row.

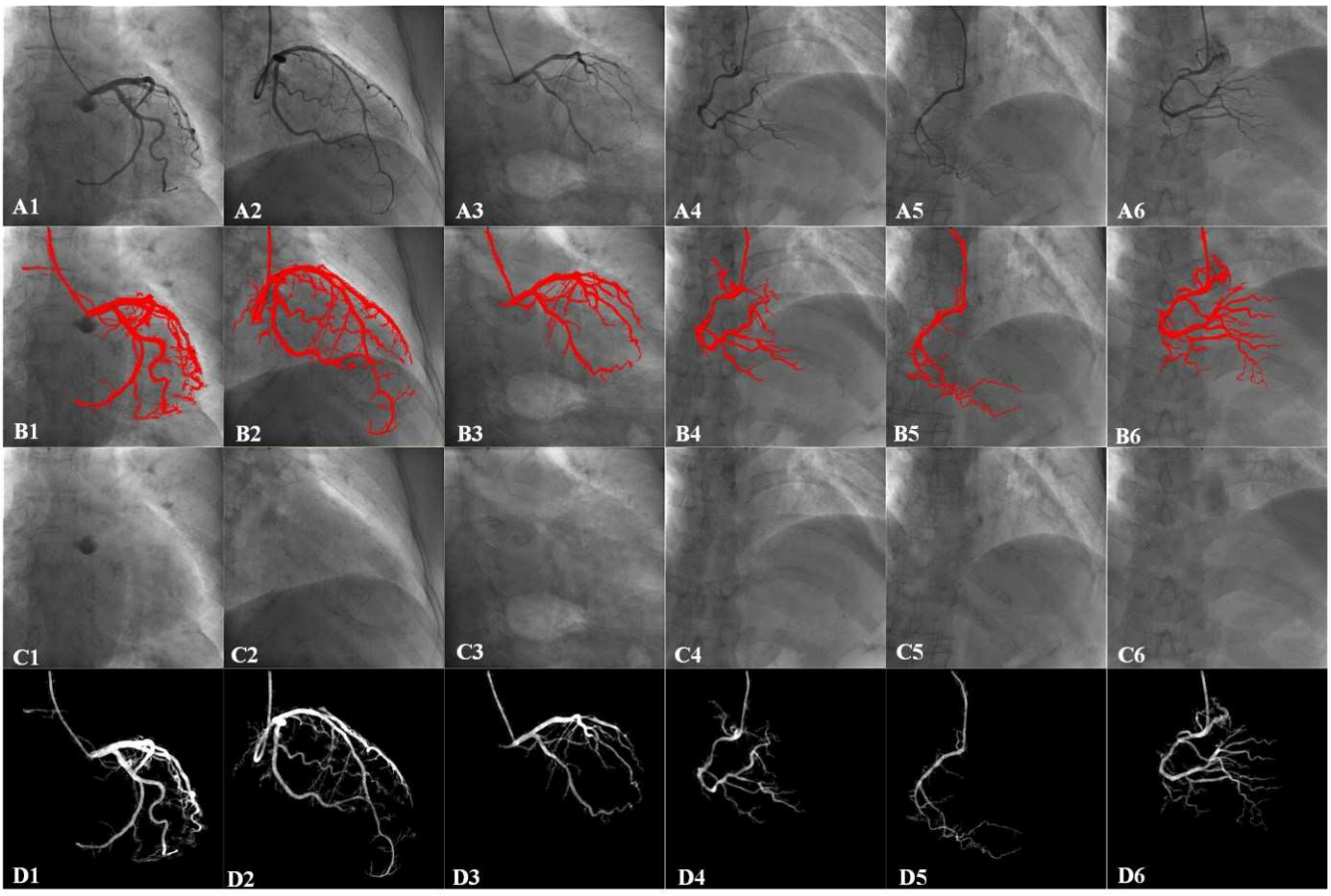

Fig. 12. Results of modules in the proposed PABSM for the enhancement of cineangiograms subject to the coronary artery of different cardiac phases from different patients. (A1-A6) Six randomly selected cineangiograms from PABSM-AED. (B1-B6) Classification results first row using the classifier. (C1-C6) Patched background. (D1-D6) Enhanced vessels. The first three columns show the cineangiograms of the left coronary artery. The last three columns display the cineangiograms of the right coronary artery.

Fig. 13 shows the comparison results of the proposed PABSM with another three up-to-date methods, namely, LBM, LPBM and BBM. Fig. 13(a) shows the two randomly selected cineangiograms from PABSM-AED, which contain the right and left coronary arteries, respectively. For PABSM, the vascular detection removes most non-vascular pixels. And the dilation of the detected region includes the local structures of vessels. After synthesizing the background, the gray values in the detected vascular regions present large difference with the values in the original cineangiogram. Hence, the proposed PABSM can provides the best results in suppressing the background noise, and preserving the detailed structures and contrast of the vessels in the images. For the other three methods, namely, LBM, LPBM and BBM, the enlarged details of the right coronary artery affirm that the original vascular structures are destroyed when intersecting, overlapping, and shortening are present for the vascular branches. The enhanced vessels appear to have blurred boundaries, possibly leading to the incorrect estimation of the vascular diameters. The enlarged details of the left coronary artery validate that the vascular edges cause serious deformation, blur, or interruption when the distance of the branches is short. In addition, LBM is sensitive to the gray value variation in the boundary of the vessels and engenders large deformations in the vascular bifurcation.

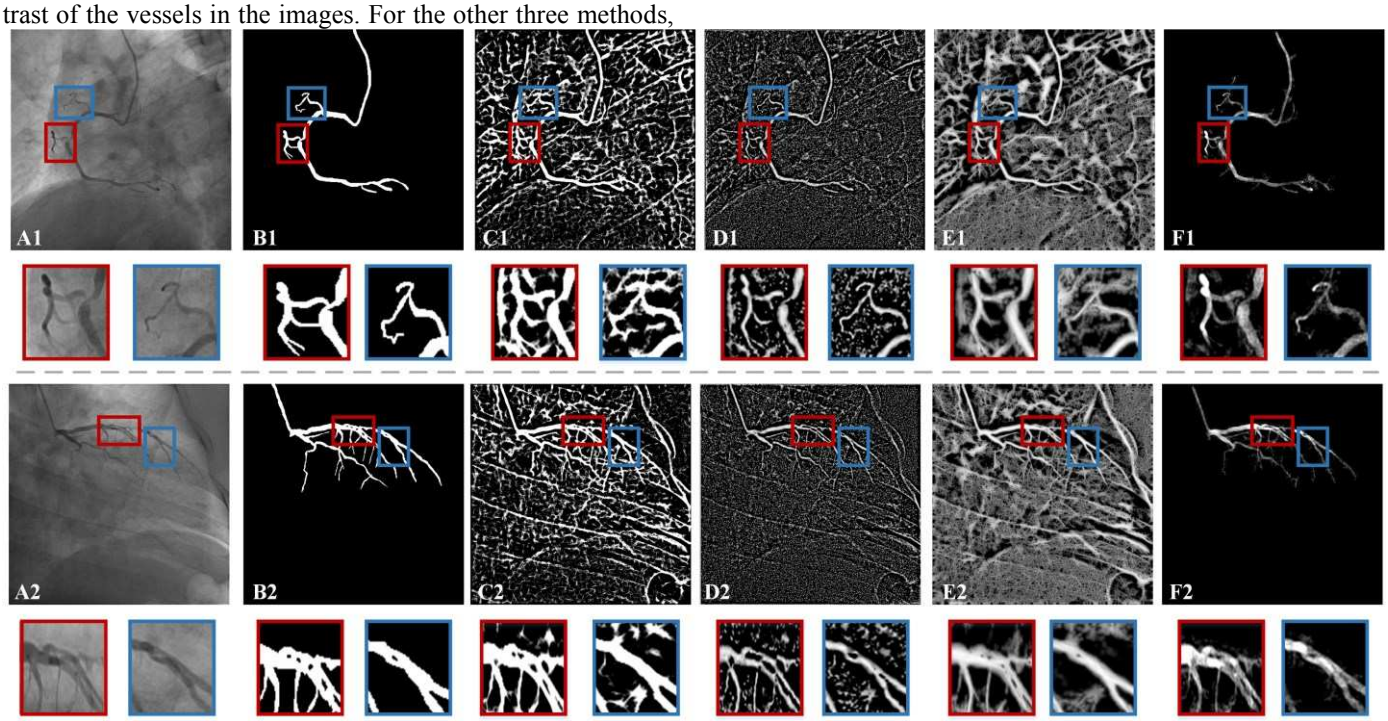

Fig. 13. Illustrative enhancement results using different enhancement methods and their partial enlarged details. (A1 and A2) the original cineangiogram. (B1 and B2) ground truth; (C1 and C2, D1 and D2, E1 and E2, F1 and F2) the enhancement results by LBM, LPBM, BBM, and PABSM, respectively. Second row: enlarged views of interest in first row; Fourth row: enlarged views of interest in third row.

Fig. 14 shows the comparison of PABSM with another three up-to-date methods, namely, MRRBM, MCCBM and SOBM. The regions with overlay vascular segments are enlarged in both images from the first column. In the first row of Fig. 14, as can be seen from the results by MRRBM, the regions of catheter and intersection of vessels and diaphragm, heart border is blurred. In addition, the contrast of vessels is low. Moreover, the subtraction results by MCCBM method present serious fracture in the heart border. Meanwhile, in the corresponding enlarged views by both MCCBM and SOBM methods, the diameters in the local overlay segments have been changed due to the artifacts. In the enlarged views of the images in the third row, local vascular segments also present non-continuity due to the artifacts. In addition, since the subtraction methods conducted on sequences cannot clean the non-vascular regions, the vessels with small diameters may not be visualized or are discontiguous. As for PABSM, the gray values of the synthesized background differ with the original cineangiograms in the vascular region, the local vascular structures are preserved.

To quantitatively compare the proposed PABSM with another six methods, namely LBM, LPBM, BBM, MRRBM, MCCBM and SOBM, we compute the precision-recall curves by segmenting the enhancement or subtraction results by different threshold values, as shown in Fig. 15. The figure reflects the quality of the threshold segmentation of different methods. According to the order of LBM, LPBM, BBM, MRRBM, MCCBM, SOBM and PABSM, the areas under the precision-recall curves of different methods are 0.0384, 0.3701, 0.4254, 0.2936, 0.4523, 0.5397 and 0.7133, respectively. The curve of PABSM is in the most upper-right part of the precision-curve space, which indicates that high segmentation quality. In addition, the position of the curve shows that PABSM effectively improves the contrast of vessels.

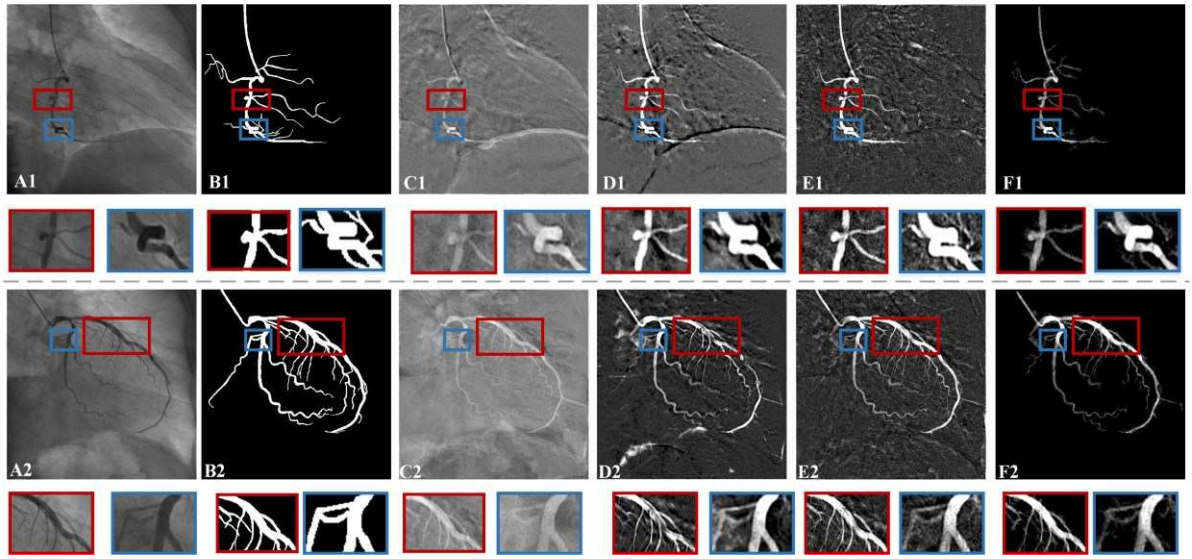

Fig. 14. Illustrative enhancement results using different enhancement methods and their partial enlarged details. (A1 and A2) the original cineangiogram. (B1 and B2) ground truth; (C1 and C2, D1 and D2, E1 and E2, F1 and F2) the enhancement results by MRRBM, MCCBM, SOBM, and PABSM, respectively. Second row: enlarged views of interest in first row; Fourth row: enlarged views of interest in third row.

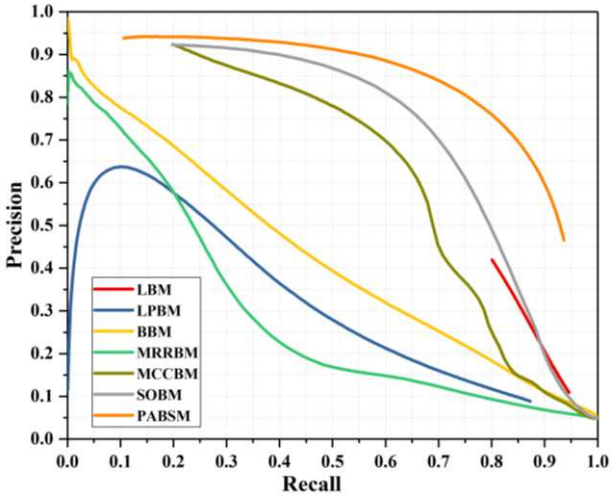

Fig. 15. Precision-recall curves of methods, namely, LBM, LPBM, BBM, MRRBM, MCCBM, SOBM and the proposed PABSM.

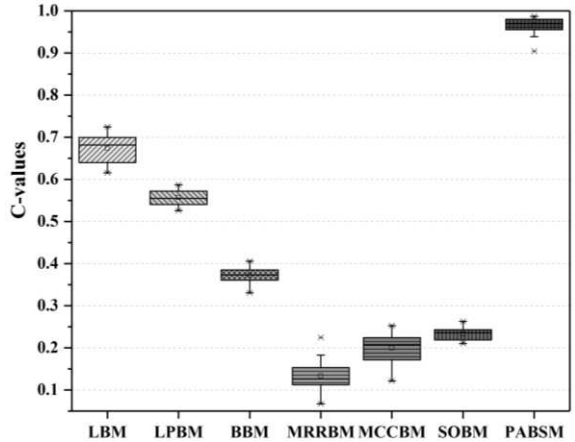

Fig. 16. Statistical comparison of the C-value for the VBM, GBM, LBM, LPBM, BBM, MCCBM, SOBM and PABSM.

Fig. 16 shows that for the 30 cineangiograms in dataset PABSM-AED, the mean and standard deviation of the C-value of LBM, LPBM, BBM, MRRBM, MCCBM, SOBM and PABSM are 0.8236 ± 0.0284, 0.7109 ± 0.0314, 0.6734 ± 0.0327, 0.5567 ± 0.0178, 0.3727 ± 0.0169, 0.1329 ± 0.0319, 0.1995 ± 0.0359, 0.2328 ± 0.0146 and 0.9659 ± 0.0185, respectively. PABSM presents a high comparative advantage, where most background noises can be removed and the vascular structures are effectively preserved.

V. Discussion

In this manuscript, we proposed a novel and robust patch-based adaptive background subtraction method for vascular enhancement and demonstrated its application in cineangiography. The classification was firstly validated by using a C-AED dataset containing 290 frames from 145 patients. The proposed subtraction method was then validated by using a PABSM-AED dataset containing 30 frames from 30 patients. In the validation of classification, we conducted 10-fold cross validation and obtained $96.55\% \pm 0.06\%$ for training sets and $92.52\% \pm 0.72\%$ for test sets. In the validation of the performance of the proposed PABSM, we obtained the area under precision-recall curve of 0.7133, and C-value of 0.9659.

For the validation of vascular enhancement performance, a comparative quantitative validation method was performed on all PABSM-AED dataset. The purpose was to determine whether the proposed technique is superior to previously developed LBM, LPBM, BBM, MRRBM, MCCBM, and SOBM. Since in the classification process, the positive sets are constructed by extracting the point-on-centerline centered patches, the classification causes under-segmentation. However, the background synthesis is based on patching method and realized after the dilation of the classification. Hence, this synthesis procedure also patches the pixels around the boundaries of the dilated vascular regions. Since the boundaries are very close to the vessels, the gray values around the boundaries present large difference with the values in the same positions in the original cineangiogram. After subtracting the background from the original cineangiogram, the vessels will be enhanced precisely. For LBM, the variation of the length of line detections may merge

close vessels, produce false responses at vessel crossovers and introduce much more noise [43]. In LPBM and BBM, morphological filters are utilized, which do not make use of unknown cross-sectional shape information or of overly long structure elements that do not handle well tortuous vessels [6]. As for MRRBM, when the motion within neighboring regions are not consistent, the deformation field computed from mask cineangiogram will cause large motion artifacts. MCCBM and SOBM are sensitive to motion artifacts caused by cardiorespiratory motion in the imaging procedure.

For the live cineangiograms in the PABSM-AED, the mean and standard deviation of the runtime are 2213 ± 940.59 s. PABSM can be divided into two parts, one is the time to compute I_1, the other is the time to compute I_3. The mean and standard variation of the first time is 2202 ± 935.72s. And the mean and standard variation of the second time is 12.23 ± 3.00s. In computing I_1, we need to compute the feature of each pixel which leads to a low time efficiency.

The limitation and challenges are as follows:

First, for each cineangiogram, the vascular detection is based on machine learning which needs to compute the feature vectors of large amounts of patches. The situation results in the low time efficiency. It is impossible to apply the subtraction method in the intra-operation. Since CNN network-based method can realize accurate vascular detection with a high time efficiency [44], an extension will be considered to detect vessels in cineangiograms by a CNN network-based method in our future work.

Second, the proposed background synthesis method requires the positions of unknown regions in advance. When the vascular segments are not classified, they cannot appear in the final subtraction cineangiogram. Hence, the vascular structures in the subtraction cineangiogram may appear fractures or missing of small-scale vascular segments. Hence, blind inpainting without knowing the vascular region should be considered for future work.

Third, considering that the proposed background synthesis is based on patches, sufficient information related to the edges is very limited. When the unknown region is large, the continuity of synthesized regions cannot be ensured. Hence, background synthesis based on deep learning should be also considered for future work.

Fourth, since the comparative methods are based on re-implementations on our datasets, the man-made bias of the results will be caused. But the comparison experiments can still validate the effectiveness of the proposed method to a certain extent.

VI. Conclusion

In summary, we proposed an automatically vascular subtraction method only based on a single live cineangiogram. Unlike previous enhancement methods, our technique can effectively preserve the integrity of vascular topological structures, particularly in complex vascular regions, such as at vascular bifurcations, intersections, and crossings. PABSM is able to remove noise caused by the non-uniform gray level distribution in the cineangiogram. PABSM is also automatic and can enhance coronary cineangiograms to diagnose and treat coronary artery diseases. In future work, a convolutional neural network-based framework will be used to realize the vascular dection and background synthesis. In this framework, both of the time efficiency and accuracy will be improved.

References:

[1] G. N. Levine, E. R. Bates, J. A. Bittl, R. G. Brindis, S. D. Fihn, L. A. Fleisher*, et al.*, "2016 ACC/AHA guideline focused update on duration of dual antiplatelet therapy in patients with coronary artery disease: a report of the American College of Cardiology/American Heart Association Task Force on Clinical Practice Guidelines," *Journal of the American College of Cardiology,* vol. 68, pp. 1082-1115, 2016.

[2] V. Kurra, S. R. Kapadia, E. M. Tuzcu, S. S. Halliburton, L. Svensson, E. E. Roselli*, et al.*, "Pre-procedural imaging of aortic root orientation and dimensions: comparison between X-ray angiographic planar imaging and 3-dimensional multidetector row computed tomography," *JACC: Cardiovascular Interventions,* vol. 3, pp. 105-113, 2010.

[3] Y. Yang, "Image segmentation and shape analysis of blood vessels with applications to coronary atherosclerosis," *Georgia Institute of Technology*, 2007.

[4] S. Moccia, E. De Momi, S. El Hadji, and L. S. Mattos, "Blood vessel segmentation algorithms—Review of methods, datasets and evaluation metrics," *Computer Methods and Programs in Biomedicine,* vol. 158, pp. 71-91, 2018.

[5] H. Ma, A. Hoogendoorn, E. Regar, W. J. Niessen, and T. van Walsum, "Automatic online layer separation for vessel enhancement in X-ray angiograms for percutaneous coronary interventions," *Medical Image Analysis,* vol. 39, pp. 145-161, 2017.

[6] Y. Zhao, Y. Zheng, Y. Liu, Y. Zhao, L. Luo, S. Yang*, et al.*, "Automatic 2-D/3-D Vessel Enhancement in Multiple Modality Images Using a Weighted Symmetry Filter," *IEEE Transactions on Medical Imaging,* vol. 37, pp. 438-450, 2018.

[7] G. Agam, S. G. Armato, and C. Wu, "Vessel tree reconstruction in thoracic CT scans with application to nodule detection," *IEEE Transactions on Medical Imaging,* vol. 24, pp. 486-499, 2005.

[8] R. Wiemker, T. Klinder, M. Bergtholdt, K. Meetz, I. C. Carlsen, and T. Bülow, "A radial structure tensor and its use for shape-encoding medical visualization of tubular and nodular structures," *IEEE Transactions on Visualization and Computer Graphics,* vol. 19, pp. 353-366, 2013.

[9] K. Krissian, G. Malandain, N. Ayache, R. Vaillant, and Y. Trousset, "Model-based detection of tubular structures in 3D images," *Computer Vision and Image Understanding,* vol. 80, pp. 130-171, 2000.

[10] M. Jiang, Q. Ji, and B. F. McEwen, "Model-based automated extraction of microtubules from electron tomography volume," *IEEE Transactions on Information Technology in Biomedicine,* vol. 10, pp. 608-617, 2006.

[11] A. F. Frangi, W. J. Niessen, K. L. Vincken, and M. A. Viergever, "Multiscale vessel enhancement filtering," *International Conference on Medical Image Computing and Computer-Assisted Intervention*, 1998, pp. 130-137.

[12] Q. Li, S. Sone, and K. Doi, "Selective enhancement filters for nodules, vessels, and airway walls in two- and three-dimensional CT scans," *Medical Physics,* vol. 30, pp. 2040-2051, 2003.

[13] G. Azzopardi, N. Strisciuglio, M. Vento, and N. Petkov, "Trainable COSFIRE filters for vessel delineation with application to retinal images," *Medical Image Analysis,* vol. 19, pp. 46-57, 2015.

[14] T. Jerman, F. Pernus, B. Likar, and Z. Spiclin, "Enhancement of Vascular Structures in 3D and 2D Angiographic Images," *IEEE Transactions on Medical Imaging,* vol. 35, pp. 2107-2118, 2016.

[15] X. Qian, M. P. Brennan, D. P. Dione, W. L. Dobrucki, M. P. Jackowski, C. K. Breuer*, et al.*, "A non-parametric vessel detection method for complex vascular structures," *Medical Image Analysis,* vol. 13, pp. 49-61, 2009.

[16] G. Läthén, J. Jonasson, and M. Borga, "Blood vessel segmentation using multi-scale quadrature filtering," *Pattern Recognition Letters,* vol. 31, pp. 762-767, 2010.

[17] S. Tang, Y. Wang, and Y.-W. Chen, "Application of ICA to X-ray coronary digital subtraction angiography," *Neurocomputing,* vol. 79, pp. 168-172, 2012.

[18] J. Yang, Y. Wang, S. Tang, S. Zhou, Y. Liu, and W. Chen, "Multiresolution elastic registration of X-ray angiography images using thin-plate spline," *IEEE Transactions on Nuclear Science,* vol. 54, pp. 152-166, 2007.

[19] Y. Bentoutou and N. Taleb, "Automatic extraction of control points for digital subtraction angiography image enhancement," *IEEE Transactions on Nuclear Science,* vol. 52, pp. 238-246, 2005.

[20] M. Nejati, S. Sadri, and R. Amirfattahi, "Nonrigid image registration in digital subtraction angiography using multilevel B-spline," *BioMed Research International,* vol. 2013, 2013.

[21] Y. Zhu, S. Prummer, P. Wang, T. Chen, D. Comaniciu, and M. Ostermeier, "Dynamic layer separation for coronary DSA and enhancement in fluoroscopic sequences," *International Conference on Medical Image Computing and Computer-Assisted Intervention*, 2009, pp. 877-884.

[22] Y. Zhu, S. Prummer, T. Chen, M. Ostermeier, and D. Comaniciu, "Coronary DSA: enhancing coronary tree visibility through discriminative learning and robust motion estimation," *Proceedings of SPIE*, 2009, pp. 72590Y-1.

[23] M. Jin, R. Li, J. Jiang, and B. Qin, "Extracting contrast-filled vessels in X-ray angiography by graduated RPCA with motion coherency constraint," *Pattern Recognition,* vol. 63, pp. 653-666, 2017.

[24] E. H. Meijering, W. J. Niessen, and M. Viegever, "Retrospective motion correction in digital subtraction angiography: a review," *IEEE Transactions on Medical Imaging,* vol. 18, pp. 2-21, 1999.

[25] C. Blondel, G. Malandain, R. Vaillant, and N. Ayache, "Reconstruction of coronary arteries from a single rotational X-ray projection sequence," *IEEE Transactions on Medical Imaging,* vol. 25, pp. 653-663, 2006.

[26] W. J. van Rooij, M. Sprengers, A. N. de Gast, J. Peluso, and M. Sluzewski, "3D rotational angiography: the new gold standard in the detection of additional intracranial aneurysms," *American Journal of Neuroradiology,* vol. 29, pp. 976-979, 2008.

[27] M. Unberath, A. Aichert, S. Achenbach, and A. Maier, "Virtual single-frame subtraction imaging," *International Conference on Image Formation in X-ray Computed Tomography*, 2016, pp. 89-92.

[28] M. Unberath, A. Aichert, S. Achenbach, and A. Maier, "Consistency-based respiratory motion estimation in rotational angiography," *Medical Physics,* vol. 44, pp. e113-e124, 2017.

[29] M. Unberath, O. Taubmann, A. Aichert, S. Achenbach, and A. Maier, "Prior-free Respiratory Motion Estimation in Rotational Angiography," *IEEE Transactions on Medical Imaging,* vol. 37, pp. 1999-2009, 2018.

[30] M. Unberath, J. Hajek, T. Geimer, F. Schebesch, M. Amrehn, and A. Maier, "Deep Learning-based Inpainting for Virtual DSA." *IEEE Nuclear Science Symposium and Medical Imaging Conference*, 2017.

[31] Y. Zheng, M. Grossman, S. P. Awate, and J. C. Gee, "Automatic Correction of Intensity Nonuniformity from Sparseness of Gradient Distribution in Medical Images," *Medical Image Computing and Computer-Assisted Intervention*, 2009, pp. 852-859.

[32] M. Haghighat, S. Zonouz, and M. Abdel-Mottaleb, "CloudID: Trustworthy cloud-based and cross-enterprise biometric identification," *Expert Systems with Applications,* vol. 42, pp. 7905-7916, 2015.

[33] R. Xiao, J. Yang, D. Ai, J. Fan, Y. Liu, G. Wang*, et al.*, "Adaptive ridge point refinement for seeds detection in X-ray coronary angiogram," *Computational and Mathematical Methods in Medicine,* vol. 2015, 2015.

[34] Z. Tu, "Probabilistic Boosting-Tree : Learning Discriminative Models for Classification, Recognition, and Clustering," *IEEE International Conference on Computer Vision,* 2005, pp. 1589-1596.

[35] T. Hastie, S. Rosset, J. Zhu, and H. Zou, "Multi-class adaboost," *Statistics and its Interface,* vol. 2, pp. 349-360, 2009.

[36] J.-B. Huang, S. B. Kang, N. Ahuja, and J. Kopf, "Image completion using planar structure guidance," *ACM Transactions on Graphics ,* vol. 33, pp. 1-10, 2014.

[37] C. Barnes, E. Shechtman, A. Finkelstein, and B. G. Dan, "PatchMatch: a randomized correspondence algorithm for structural image editing," *ACM Special Interest Group on Graphics and Internative Techniques*, 2009, pp. 1-11.

[38] G. Yang, Y. Hu, X. Huang, H. Shu, and C. Toumoulin, "Simulation environment of X-ray rotational angiography using 3D+t coronary tree model," *Annual International Conference of the IEEE Engineering in Medicine and Biology Society*, 2012, pp. 629-632.

[39] W. Segars, G. Sturgeon, S. Mendonca, J. Grimes, and B. M. Tsui, "4D XCAT phantom for multimodality imaging research," *Medical Physics,* vol. 37, pp. 4902-4915, 2010.

[40] S. Song, J. Yang, J. Fan, W. Cong, D. Ai, Y. Zhao*, et al.*, "Geometrical force constraint method for vessel and x-ray angiogram simulation," *Journal of X-ray Science and Technology,* vol. 24, pp. 87-106, 2016.

[41] U. T. Nguyen, A. Bhuiyan, L. A. Park, and K. Ramamohanarao, "An effective retinal blood vessel segmentation method using multi-scale line detection," *Pattern Recognition,* vol. 46, pp. 703-715, 2013.

[42] M. Nejati and H. Pourghassem, "Multiresolution image registration in digital X-Ray angiography with intensity variation modeling," *Journal of Medical Systems,* vol. 38, p. 10, 2014.

[43] Y. Hou, "Automatic segmentation of retinal blood vessels based on improved multiscale line detection," *Journal of Computing Science and Engineering*, vol. 8, pp. 119-128, 2014.

[44] J. Fan, J. Yang, Y. Wang, S. Yang, D. Ai, Y. Huang, H. Song, A. Hao and Y.T. Wang, "Multichannel Fully Convolutional Network for Coronary Artery Segmentation in X-ray Angiograms," *IEEE Access*, vol. 6, pp. 44635-44643, 2018.